Dynamic structure factor of two-dimensional Fermi superfluid with Rashba spin-orbit coupling

Huaisong Zhao [1], Xu Yan [2,*], Shi-Guo Peng [3,†] and Peng Zou [1,‡]

[1]*College of Physics, Qingdao University, Qingdao 266071, China*

[2]*Industrial Research Institute of Nonwovens and Technical Textiles, Shandong Center for Engineered Nonwovens, College of Textiles and Clothing, Qingdao University, Qingdao 266071, China*

[3]*State Key Laboratory of Magnetic Resonance and Atomic and Molecular Physics, Innovation Academy for Precision Measurement Science and Technology, Chinese Academy of Sciences, Wuhan 430071, China*

We theoretically calculate the dynamic structure factor of a two-dimensional Rashba-type spin-orbit-coupled (SOC) Fermi superfluid with the random phase approximation and analyze the main characters of dynamical excitation shown by both density and spin dynamic structure factors during a continuous phase transition between a Bardeen-Cooper-Schrieffer superfluid and a topological superfluid. Generally we find three different excitations, including collective phonon excitation, two-atom molecular and atomic excitations, and pair-breaking excitations due to the two-branch structure of the quasiparticle spectrum. It should be emphasized that collective phonon excitation is overlapped with a gapless DD-type pair-breaking excitation at the critical Zeeman field h_c and is imparted a finite width to phonon peak when the transferred momentum $\boldsymbol{q}$ is around the Fermi vector k_F. At a much larger transferred momentum ($\boldsymbol{q} = 4k_F$), the pair-breaking excitation happens earlier than two-atom molecular excitation, which is different from the conventional Fermi superfluid without the SOC effect.

I. INTRODUCTION

Finding and distinguishing exotic matter states are interesting and important tasks in quantum many-body physics [1,2]. In atomic physics, the strategy that analyzing the atomic spectrum structure shown by all possible electronic transitions between atomic energy levels has been verified to be an effective way to distinguish chemical elements. All spectra consist of dynamical excitation information, which can be described by the optical spectrum dynamic structure factor. In quantum many-body physics, many particles interplay with each other and arrive at rich equilibrium matter states. Since the realization of the spin-linear (angular) momentum coupling effect in ultracold atomic gases [3–13], it has been possible to investigate many exotic matter states, such as two types of stripe phase with discrete translational or rational symmetry [14–16], the topological state [17–19], etc., in these highly controllable systems. Naturally it is interesting to know whether it is possible to find a universal way to identify all these matter states with dynamical excitation information.

The dynamic structure factor, which is related to the imaginary part of the response function in the momentum-energy representation, is an important many-body physical quantity and includes rich dynamics about the system in a certain matter state [20]. Experimentally the dynamic structure factor can be measured by a two-photon Bragg scattering technique [21–25], in which two Bragg laser beams can transfer a selected transferred momentum $\boldsymbol{q}$ and energy ω to perturb the system. After this Bragg perturbation, the dynamic structure factor can be obtained by measuring the center-of-mass velocity of the system [26]. In a small transferred momentum $\boldsymbol{q}$, some momentum-related collective modes, like Goldstone phonons [22,27,28], second sound [29,30], Higgs mode [31–37], and Leggett excitation [38,39], can be observed. At a large $\boldsymbol{q}$, the dynamics is dominated by the single-particle excitation, including not only the Cooper pair-breaking excitation but also the ideal (or interaction-revised) atomic or molecular excitation [27,40]. All these dynamics consist of the dynamical character of the system in a specific matter state and may display different dynamical behaviors during phase transition. So it is interesting to study these dynamical characters of the system in different matter states according to the dynamic structure factor and to check the feasibility to identify the matter state by the dynamic structure factor. In our previous work, we found that the dynamic structure factor can display different dynamical behaviors in a few phase transitions [41–43].

In this paper, we theoretically investigate a two-dimensional (2D) Rashba-type spin-orbit-coupled (SOC) Fermi superfluid, which can experience a continuous phase transition from a conventional Bardeen-Cooper-Schrieffer (BCS) superfluid to a topological superfluid by continuously varying the Zeeman field [44]. We numerically calculate the dynamic structure factor of this system with the random phase approximation [45,46] and try to find its main dynamical excitation character during phase transition. We find the dynamic structure factor presents rich excitation signals, including collective phonon excitation, molecular or atomic excitations, and four kinds of pair-breaking excitations due to the

---

*qdyanx@qdu.edu.cn

†pengshiguo@wipm.ac.cn

‡phy.zoupeng@gmail.com

two-branch structure of the quasiparticle spectrum. Among all these excitations, the collective phonon excitation requires the smallest excitation energy in both the BCS and the topological superfluid. At the critical point of the phase transition, one of the pair-breaking excitations becomes a gapless excitation. It overlaps with the phonon excitation and imparts a finite expansion width to the phonon peak in a certain transferred momentum. This paper is organized as follows. In the next section, we use the motion equation of Green's function to introduce the microscopic model of a 2D Fermi superfluid with the Rashba SOC effect, outline the mean-field approximation, and show how to calculate the response function with the random phase approximation. We give results of the dynamic structure factor of both BCS and topological superfluids in Sec. III, and we give our conclusions and outlook in Sec. IV. Some calculation details are listed in the Appendix.

II. METHODS

A. Model and Hamiltonian

We consider a uniform 2D Fermi gas subject to a Rashba SOC potential $V_{soc} = -i\lambda(\partial_y + i\partial_x)$ with strength λ and a Zeeman field h. The system can be described by the model Hamiltonian

$$H = \int d^2r \left[\sum_\sigma \mathcal{H}_\sigma^S + \mathcal{H}_{SOC} + \mathcal{H}_{int} \right]. \quad (1)$$

Here $\mathcal{H}_\sigma^S = \psi_\sigma^\dagger[-\nabla^2/2m - \mu - h\sigma_z]\psi_\sigma$ is the single-particle Hamiltonian of spin-σ component particles with mass m in reference to the chemical potential μ, and $\psi_\sigma(\psi_\sigma^\dagger)$ is the annihilation (generation) operator. $\mathcal{H}_{SOC} = \psi_\uparrow^\dagger V_{soc} \psi_\downarrow + \text{H.c.}$ is the Rashba SOC Hamiltonian, and it should be noted that the strength λ of the SOC effect is isotropic in the 2D XY plane. $\mathcal{H}_{int} = U\psi_\uparrow^\dagger\psi_\downarrow^\dagger\psi_\downarrow\psi_\uparrow$ describes the contact interaction between opposite spins, in which the strength U should be regularized via $1/U = -\sum_k 1/(k^2/m + E_a)$. E_a is the binding energy of the two-body bound state and is often used to demonstrate the interaction strength in the 2D system [47]. Here and in the following, we have set $\hbar = k_B = 1$ for simplicity. Since we consider a uniform system with the bulk density n_0, the inverse of the Fermi wave vector $k_F = \sqrt{2\pi n_0}$ and the Fermi energy $E_F = k_F^2/2m$ are used as length and energy units, respectively.

A standard mean-field treatment is carried out to the interaction Hamiltonian $\mathcal{H}_{int}$ with the usual definition of order parameter $\Delta = -U\langle\psi_\downarrow\psi_\uparrow\rangle$. After Fourier transformation to the mean-field model Hamiltonian, we can obtain its expression in the momentum representation, which reads

$$H_{mf} = \sum_{k\sigma} (\xi_k - h\sigma_z) c_{k\sigma}^\dagger c_{k\sigma}$$

$$+ \sum_k [\lambda(k_y + ik_x)c_{k\uparrow}^\dagger c_{k\downarrow} + \text{H.c.}]$$

$$- \sum_k [\Delta c_{k\uparrow}^\dagger c_{-k\downarrow}^\dagger + \Delta^* c_{-k\downarrow}c_{k\uparrow}], \quad (2)$$

with $\xi_k = k^2/2m - \mu$. Usually the order parameter Δ is a complex number. However, U(1) symmetry is spontaneously broken in the ground state of the system, and the value for the

phase of Δ is pushed to choose a random number. Here we just set $\Delta = \Delta^*$. The exact diagonalization of the mean-field Hamiltonian H_{mf} can be solved with the motion equation of Green's functions. Finally we get six independent Green's functions, which are as follows:

$$G_1(k, \omega) \equiv \langle\langle c_{k\uparrow}|c_{k\uparrow}^\dagger\rangle\rangle = \sum_l [G_1]_k^l/(\omega - E_k^l),$$

$$G_2(k, \omega) \equiv \langle\langle c_{k\downarrow}|c_{k\downarrow}^\dagger\rangle\rangle = \sum_l [G_2]_k^l/(\omega - E_k^l),$$

$$\Gamma(k, \omega) \equiv \langle\langle c_{k\uparrow}|c_{-k\downarrow}\rangle\rangle = \sum_l [\Gamma]_k^l/(\omega - E_k^l),$$

$$S(k, \omega) \equiv \langle\langle c_{k\downarrow}|c_{k\uparrow}^\dagger\rangle\rangle = \sum_l [S]_k^l/(\omega - E_k^l),$$

$$F_1(k, \omega) \equiv \langle\langle c_{k\uparrow}|c_{-k\uparrow}\rangle\rangle = \sum_l [F_1]_k^l/(\omega - E_k^l),$$

$$F_2(k, \omega) \equiv \langle\langle c_{k\downarrow}|c_{-k\downarrow}\rangle\rangle = \sum_l [F_2]_k^l/(\omega - E_k^l), \quad (3)$$

where $l = \pm1$ and ±2 denotes respectively all four important quasiparticle energy spectra $E_k^{(+1)} = -E_k^{(-1)} = U_k$ and $E_k^{(+2)} = -E_k^{(-2)} = D_k$. U_k and D_k are respectively the up- and down-branch positive quasiparticle spectra:

$$U_k = \sqrt{E_k^2 + h^2 + k^2\lambda^2 + 2\sqrt{E_k^2 h^2 + \xi_k^2 k^2\lambda^2}}, \quad (4)$$

$$D_k = \sqrt{E_k^2 + h^2 + k^2\lambda^2 - 2\sqrt{E_k^2 h^2 + \xi_k^2 k^2\lambda^2}}, \quad (5)$$

with $E_k = \sqrt{\xi_k^2 + \Delta^2}$. The Green's functions S, F_1, and F_2 come from the Rashba SOC Hamiltonian, and they are the odd functions of momentum k, which are the even functions in the Raman SOC case. These single-particle spectra (U_k and D_k) do greatly influence the static and dynamical properties of the ground state. All expressions related to $[G_1]_k^l$, $[G_2]_k^l$, $[\Gamma]_k^l$, $[S]_k^l$, $[F_1]_k^l$, and $[F_2]_k^l$ are given in the Appendix.

Based on the spectrum theorem, it is also easy to get all equations of all physical quantities with the above Green's functions. For example, we obtain the following spin-up and spin-down density equations,

$$n_1 = \sum_k \langle c_{k\uparrow}^\dagger c_{k\uparrow}\rangle = -\frac{1}{\pi}\sum_k \int d\omega \frac{\text{Im}[G_1(k, \omega)]}{e^{\omega/T} + 1}, \quad (6)$$

$$n_2 = \sum_k \langle c_{k\downarrow}^\dagger c_{k\downarrow}\rangle = -\frac{1}{\pi}\sum_k \int d\omega \frac{\text{Im}[G_2(k, \omega)]}{e^{\omega/T} + 1}, \quad (7)$$

and the order parameter equation

$$\frac{\Delta}{U} = -\sum_k \langle c_{-k\downarrow}c_{k\uparrow}\rangle = \frac{1}{\pi}\sum_k \int d\omega \frac{\text{Im}[\Gamma(k, \omega)]}{e^{\omega/T} + 1}, \quad (8)$$

with the Green's functions G_1, G_2, and Γ in Eq. (3) at the temperature T. By self-consistently solving the density and order parameter equations, the value of the chemical potential μ and the order parameter Δ can be numerically calculated.

In this paper, we just consider the zero temperature case and take the binding energy as $E_a = 0.5E_F$ and the SOC strength as $\lambda k_F/E_F = 1.5$. As shown in Fig. 1, the system experiences a phase transition from a BCS superfluid to a
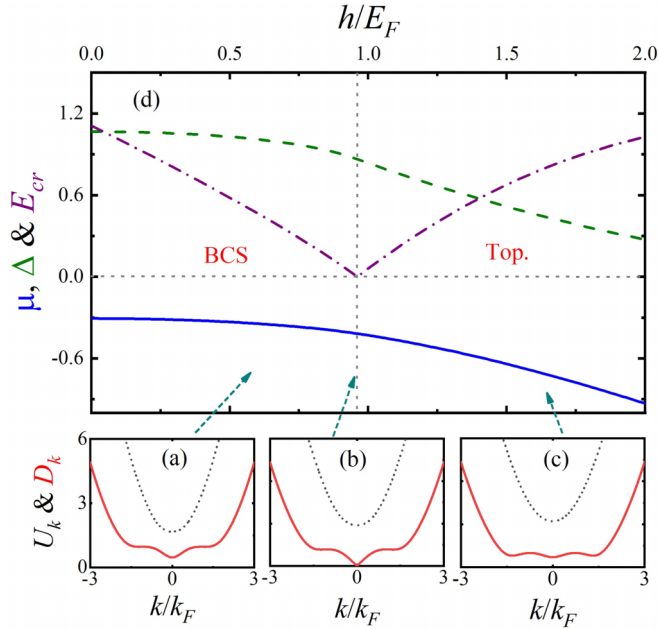
FIG. 1. Two types of single-particle excitation spectra U_k (black short-dotted line) and D_k (red solid line) at different Zeeman fields: (a) $h = 0.6E_F$, (b) $h = 0.96E_F$, and (c) $h = 1.3E_F$. (d) The distribution of chemical potential (blue solid line), order parameter (olive dashed line), and $E_{cr} = |h - \sqrt{\mu^2 + \Delta^2}|$ (purple dash-dotted line) at different Zeeman fields h during a continuous phase transition from a BCS superfluid to a topological superfluid. A gray vertical dotted line marks the location of a critical value of the Zeeman field $h_c = 0.96E_F$ at $E_a = 0.5E_F$ and $\lambda k_F/E_F = 1.5$.

topological superfluid by increasing the Zeeman field h over a critical value $h_c = 0.96E_F$. This is a continuous phase transition, which is displayed by the smooth variation of the chemical potential μ and the order parameter Δ with the Zeeman field h. The critical Zeeman field h_c is determined by the zero value of $E_{cr} = |h - \sqrt{\mu^2 + \Delta^2}|$. When $h = h_c$, the minimum of D_k touches zero at momentum $\boldsymbol{k} = 0$ [red line in Fig. 1(b)]. By continuously increasing Zeeman field h from $h < h_c$ to $h > h_c$, the value of the second-order local minimum in the lower-branch spectrum D_k at a nonzero momentum $\boldsymbol{k}$ will experience a variation from the situation that is much larger than the global minimum at $\boldsymbol{k} = 0$ in the BCS regime to the case of almost the same value of the global one at $\boldsymbol{k} = 0$ in the topological regime, while the spectrum structure of U_k does not change too much. We have checked that the continuous phase transition mentioned above will be present in a quite large parameter space of SOC strength λ, except a weak SOC strength of $\lambda k_F/E_F < 0.4$ where the parameter space of the topological superfluid is depressed to almost vanishing and makes the phase transition to be a first order one from a trivial superfluid to normal state.

Next we discuss the dynamical excitation of this system.

B. Response function and random phase approximation

At zero temperature, the interacting system comes into a superfluid state and induces four different densities. Besides the normal spin-up density $n_1 = \langle \psi_\uparrow^\dagger \psi_\uparrow \rangle$ and spin-down

density $n_2 = \langle \psi_\downarrow^\dagger \psi_\downarrow \rangle$, the pairing physics of two spins generates the other anomalous density $n_3 = \langle \psi_\downarrow \psi_\uparrow \rangle$ and its conjugate counterpart $n_4 = \langle \psi_\uparrow^\dagger \psi_\downarrow^\dagger \rangle$. The interaction between particles makes these four densities couple closely with each other. Any fluctuation in each kind of density will influence other densities and generate a non-negligible density fluctuation of them. This physics plays a significant role in the dynamical excitation of the system, which demonstrates the importance and necessity of the term in the Hamiltonian beyond mean-field theory. The random phase approximation has been verified to be a good way to treat the fluctuation term of the Hamiltonian [45]. Comparing with experiments, it can even obtain some quantitatively reliable predictions in three-dimensional Fermi superfluid [48,49]. Its prediction also qualitatively agrees with quantum Monte Carlo data in a 2D Fermi system [35,50]. The random phase approximation treats the fluctuation of the Hamiltonian as parts of an effective external potential [42,46] and finds the response function χ of the system is connected to its mean-field approximation χ^0, whose calculation is relatively easier, by the following equation:

$$\chi = \frac{\chi^0}{1 - \chi^0 M_I U}, \tag{9}$$

where

$$M_I = \begin{bmatrix} 0 & 1 & 0 & 0 \\ 1 & 0 & 0 & 0 \\ 0 & 0 & 0 & 1 \\ 0 & 0 & 1 & 0 \end{bmatrix}$$

is a constant matrix reflecting the coupling situation of four kinds of densities.

Next we introduce the expression of the mean-field response function χ^0, which is a 4×4 matrix,

$$\chi^0 = \begin{bmatrix} \chi_{11}^0 & \chi_{12}^0 & \chi_{13}^0 & \chi_{14}^0 \\ \chi_{21}^0 & \chi_{22}^0 & \chi_{23}^0 & \chi_{24}^0 \\ \chi_{31}^0 & \chi_{32}^0 & \chi_{33}^0 & \chi_{34}^0 \\ \chi_{41}^0 & \chi_{42}^0 & \chi_{43}^0 & \chi_{44}^0 \end{bmatrix}. \tag{10}$$

Here its ij matrix element is defined by $\chi_{ij}^0(\boldsymbol{r}_1, \boldsymbol{r}_2, \tau, 0) \equiv -\langle \hat{n}_i(\boldsymbol{r}_1, \tau) \hat{n}_j(\boldsymbol{r}_2, 0) \rangle$; density operators $\hat{n}_i$ and $\hat{n}_j$ were introduced at the beginning of this subsection. In the uniform system, all response function elements are only the function of the 2D relative coordinate $\boldsymbol{r} = \boldsymbol{r}_1 - \boldsymbol{r}_2$ and time τ. So a generalized coordinate $R = (\boldsymbol{r}, \tau)$ is used to go on discussing. Based on Wick's theorem, we should consider all possible two-operator contraction terms, which are all related to the six independent Green's functions of Eq. (3). We find that the mean-field response function $\chi^0 = A + B$, in which A is only connected to the Green's functions G_1, G_2, and Γ, while B is connected to the SOC Green's functions S, F_1, and F_2. For example, in the spatial and time representation, $\chi_{11}^0(R) \equiv -\langle \hat{n}_1(\boldsymbol{r}_1, \tau) \hat{n}_1(\boldsymbol{r}_2, 0) \rangle = A_{11}(R) + B_{11}(R)$, where $A_{11}(R) = G_1(-R)G_1(R)$ and $B_{11}(R) = -F_1^*(-R)F_1(R)$. After Fourier transformation to Green's functions, we obtain the expression of all matrix elements in the momentum-energy representation

$$\chi^0(\boldsymbol{q}, \omega) = A(\boldsymbol{q}, \omega) + B(\boldsymbol{q}, \omega), \tag{11}$$

where

$$A = \begin{bmatrix} A_{11}, & A_{12}, & A_{13}, & A_{14} \\ A_{12}, & A_{22}, & A_{23}, & A_{24} \\ A_{14}, & A_{24}, & -A_{12}, & A_{34} \\ A_{13}, & A_{23}, & A_{43}, & -A_{12} \end{bmatrix}$$

has nine independent matrix elements, and

$$B = \begin{bmatrix} B_{11}, & B_{12}, & B_{13}, & B_{14} \\ B_{21}, & B_{22}, & B_{23}, & B_{24} \\ B_{31}, & B_{32}, & B_{33}, & B_{34} \\ B_{41}, & B_{42}, & B_{43}, & B_{44} \end{bmatrix}.$$

All expressions of these matrix elements are listed in the Appendix. The numerical calculation of all the above matrix elements requires a two-dimensional integral, which makes the numerical calculations here much heavier than those of the one-dimensional SOC system [42].

C. Dynamic structure factor

With Eqs. (9) and (11), we can obtain the expression of both the total density response function $\chi_n \equiv \chi_{11} + \chi_{22} + \chi_{12} + \chi_{21}$ and the spin density response function $\chi_s \equiv \chi_{11} + \chi_{22} - \chi_{12} - \chi_{21}$. χ_n reflects the density response of the system, while χ_s shows the spin density response in two-spin components. Based on the fluctuation and dissipation theorem, their imaginal parts are connected to density and spin dynamic structure factors by

$$S_{n/s} = -\frac{1}{\pi} \frac{1}{1 - e^{-\omega/T}} \text{Im}[\chi_{n/s}]. \tag{12}$$

III. RESULTS

In the following discussions, we focus on an interaction binding energy of $E_a = 0.5E_F$ and a typical SOC strength of $\lambda k_F/E_F = 1.5$ at zero temperature. These parameters are the same as those in Fig. 1. As introduced before, the isotropy of the Rashba SOC effect induces that the Hamiltonian equation (1) is also isotropic, which means the direction of the transferred momentum q can make no difference to the dynamical excitation of the system, so we just set q along the positive direction of X axis. And the dynamical excitation of the system is also rotation invariant in the 2D XY plane.

We numerically calculate the density (left column) and spin (right column) dynamic structure factors, as shown in Fig. 2, in the phase transition from a BCS superfluid (top two panels), across the critical regime (middle two panels), and then to a topological superfluid (bottom two panels). Generally we investigate a full dynamical excitation in different transferred momenta q, including the low-energy (or momentum) collective excitation and the high-energy (or momentum) single-particle excitation. The white dotted lines mark the location of three types of the minimum energy needed to break a Cooper pair, which will be introduced later.

A. Collective and single-particle excitation

At a low transferred energy ω, it is easy to investigate the collective excitation [51]. By continuously increasing the transferred momentum q from zero, we initially see a
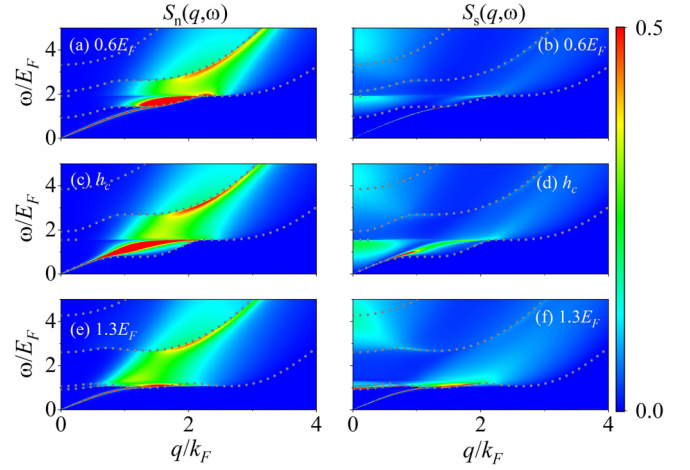
FIG. 2. The density (left column) and spin (right column) dynamic structure factors at three typical different Zeeman fields $h = 0.6E_F$, h_c, and $1.3E_F$. The dotted lines are the same lines as described in Fig. 4, which reflect all kinds of threshold energy needed to break a Cooper pair.

gapless phonon excitation in both the density and spin dynamic structure factors. As shown in Fig. 3, the velocity of collective phonon excitation almost does not change during this continuous phase transition, which is different from the first order one in 1D Raman SOC Fermi superfluid [42]. When the transferred momentum q is large enough, this phonon excitation gradually merges into the continuous single-particle excitation. Specially in the critical regime $h = h_c$, the minimum of the lower single-particle spectrum D_k touches zero [Fig. 1(b)], which induces a gapless pair-breaking excitation at the same location as the collective phonon excitation and gives a finite expansion width to the phonon excitation.

When the transferred energy ω is large enough, the excitation of the system is dominated by the single-particle excitation. A pair-breaking of Cooper pairs will occur and make pairs be broken into free Fermi atoms. Indeed, much

FIG. 3. The sound velocity c_s at different Zeeman fields h.

FIG. 4. All kinds of threshold energy of pair-breaking excitation in different momenta at (a) $h = 0.6E_F$, (b) $h = 0.96E_F$, and (c) $h = 1.3E_F$. Olive solid line: $D_k \leftrightarrow D_{k+q}$. Red dotted line: $D_k \leftrightarrow U_{k+q}$ and $U_k \leftrightarrow D_{k+q}$. Blue dashed line: $U_k \leftrightarrow U_{k+q}$.

FIG. 5. The density (gray) and spin (magenta) dynamical structure factors at transferred momentum $q = 4k_F$. (a) $h = 0.6E_F$ in the BCS superfluid, (b) $h = 0.96E_F$ at the transition point, and (c) $h = 1.3E_F$ in the topological superfluid.

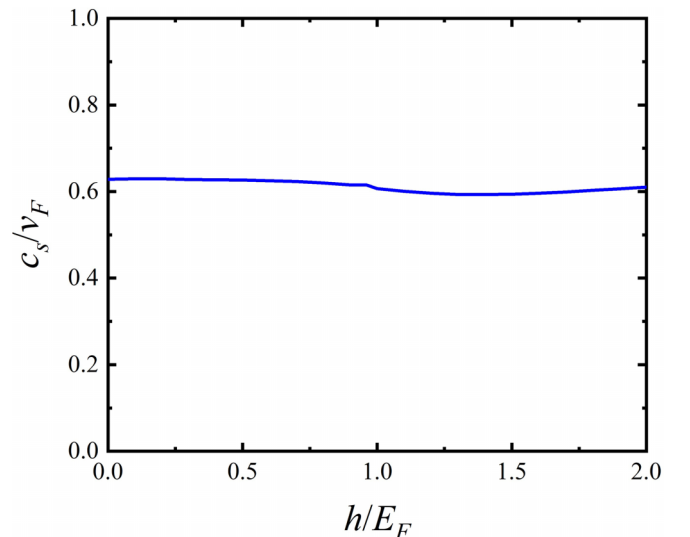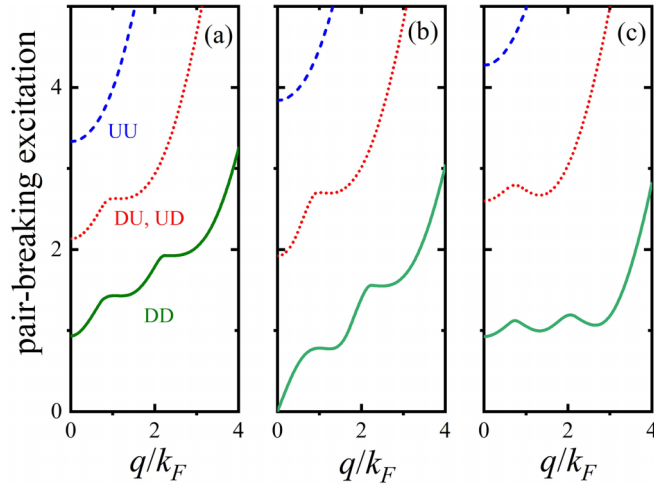of the dynamical excitation in Fig. 2 is dominated by this pair-breaking effect. In the density dynamic structure factor S_n, this effect usually is very obvious in a relatively large transferred momentum $q > k_F$, where the collective excitation is strongly depressed. Different from the conventional Fermi superfluid, this single-particle excitation takes up a large regime in the spin dynamic structure factor S_s, even for a small or zero transferred momentum q. To understand this, it is necessary to study the threshold energy needed to break a Cooper pair. This pair-breaking excitation is related to two branches of quasiparticle spectra U_k and D_k. The two atoms forming a Cooper pair can come from the same or the opposite branch of a single-particle spectrum. This two-branch spectrum structure generates four kinds of mechanisms to break a Cooper pair, namely, the DD, DU, UD, and UU types. The minimum energy at a certain momentum q to break a pair is $\min[D_k + D_{k+q}]$, $\min[D_k + U_{k+q}]$, $\min[U_k + D_{k+q}]$, or $\min[U_k + U_{k+q}]$. Here the DU and UD excitations are overlapped with each other, and finally display three kinds of pair-breaking excitation regimes. The minimum energy in these pair-breaking excitations are shown in the three panels of Fig. 4 and are also displayed by the dotted lines in Fig. 2. The bottom olive line denotes the DD-type minimum energy ($\min[D_k + D_{k+q}]$) needed to break a Cooper pair at a certain q, and atoms forming a Cooper pair are both from the down-branch quasiparticle spectrum D_k. Generally this value is always larger than zero in both a BCS superfluid [Fig. 4(a)] and a topological superfluid [Fig. 4(c)]. However it will touch zero at the critical Zeeman field $h = 0.96E_F$ [Fig. 4(b)], which is an important signal of this continuous phase transition. The red line denotes the minimum energy of cross-spectrum excitation (DU and UD types). The two atoms in a pair come from different branches of the spectrum. This excitation starts from the $\min[D_k + U_{k+q}]$, and it requires an energy higher than the DD one. This cross-spectrum excitation also reflects the coupling effect between spin and orbital motion, and it is much easier to be observed in the spin dynamic structure
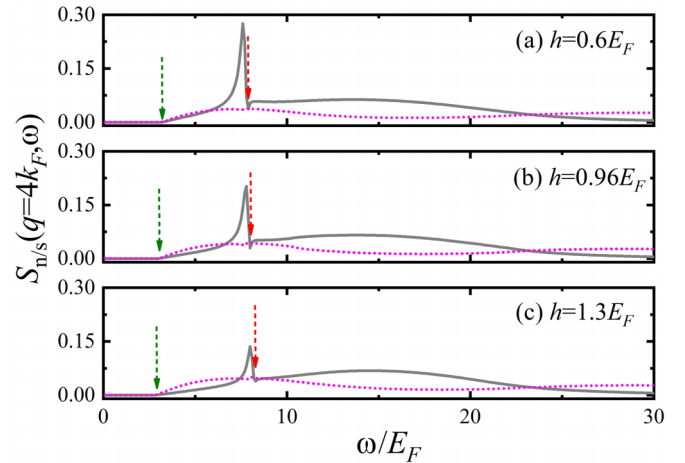
factor than that in density one. The blue dashed line is the minimum energy in the UU excitation. Its energy is the largest among three kinds of pair-breaking excitation; however, the excitation signal of the UU excitation is the weakest.

Besides all the global minima discussed above, there are also some possible local minima in these pair-breaking excitations, which generate some edges in the dynamic structure factor. For example, some horizon edges emerge when ω is a little lower than $2E_F$ in the dynamic structure factor of Fig. 2, which is from the local minimum of the DD-type pair-breaking excitation.

To better understand the dynamical excitation in these colorful panels, we also discuss the dynamic structure factor at a fixed transferred momentum q.

B. Dynamic excitation at a constant momentum q

For a large transferred momentum $q \gg k_F$, the dynamic structure factor is dominated by the single-particle excitation. As shown in Fig. 5, we investigate the density and spin dynamic structure factors at $q = 4k_F$ between BCS and topological superfluid. In all three panels, we always find a high excitation signal in the density dynamic structure factor (gray solid lines) around $\omega = 8E_F$. In fact, it is the molecular Cooper-pair excitation, whose dispersion relation can be easily explained by $\varepsilon_k = q^2/2M$, and $M = 2m$ is the mass of a two-atom molecule. Also the single-atom excitation arrives at its maximum around $q^2/2m \approx 16E_F$ here. The olive and red arrows respectively mark the threshold energy to break a Cooper pair in the DD- and DU-type (or UD-type) excitations. Different from the 3D crossover Fermi superfluid [40], the Rashba-SOC effect makes DD pair-breaking excitation happen earlier than molecular excitation, no matter the value of the Zeeman field h.

When taking the transferred momentum $q = 2k_F$, the collective phonon has already merged into the regime of single-particle excitation. The dynamic structure factor is dominated by strong signals of pair-breaking excitation. As

FIG. 6. The density (gray line) and spin (magenta line) dynamical structure factors at the transferred momentum $q = 2k_F$. The parameters in these three panels are the same as those in Fig. 5.
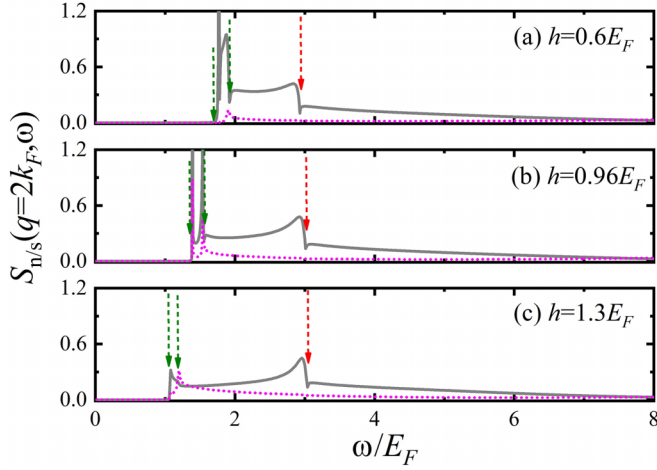

FIG. 8. The density (gray line) and spin (magenta line) dynamical structure factors at the transferred momentum $q = 0.5k_F$. The parameters in these three panels are the same as those in Fig. 5.

shown in Fig. 6, both curves of S_n and S_s have many twists, which means they exhibit rich oscillations, and the two-olive arrows respectively mark the global (left) and local (right) minimum energy to break a Cooper pair according to the DD-type excitation, and one red-dashed arrow marks the minimum energy of the DU-type (or UD-type) excitation. In all three panels, small peaks (left side of the red arrow) in the density dynamic structure factor display the two-atom molecule excitation around $\omega = 2.9E_F$, and the obvious deviation from the dispersion line $\varepsilon_k = q^2/2M = 4E_F$ is due to its coupling effect to pair-breaking excitation in this relative weak transferred momentum ($q = 2k_F$).

For a transferred momentum q at the order of the Fermi wave vector k_F (or smaller than k_F), the collective phonon excitation can be separated from the pair-breaking excitation and happens at an energy smaller than that of the pair-breaking effect. In panels (a) and (c) of Figs. 7 and 8, strong sharp peaks are shown on the leftmost side of the dynamic structure

factor, whose excitation energy is smaller than the global minimum energy of the DD-type pair-breaking excitation. And the separation energy between the phonon excitation and the DD-type threshold excitation is relatively small in the topological superfluid ($h = 1.3E_F$) since it has an order parameter Δ weaker than that in the BCS superfluid ($h = 0.6E_F$). However, at the point of phase transition $h = 0.96E_F$ [shown by panel (b) of Figs. 7 and 8], the phonon excitation is just overlapped with the beginning of the gapless DD-type pair-breaking excitation, and give a finite width to the phonon peak at $q = 1k_F$ [Fig. 7(b)]. At $q = 0.5k_F$, although these two excitations are still mixed with each other at $h = 0.96E_F$, this small transferred momentum q generates a relative weaker strength of the DD excitation. The phonon excitation is still very sharp in the density dynamic structure factor, and the spin dynamic structure factor can help to track the signal of the DD excitation and display a bump structure closely following the phonon peak.

IV. CONCLUSIONS AND OUTLOOK

In summary, we numerically calculate the density and spin dynamic structure factors of a 2D Rashba SOC Fermi superfluid with the random phase approximation during a continuous phase transition between BCS and topological superfluids. The dynamic structure factor presents rich excitation signals, including collective phonon excitation, molecular or atomic excitations, and pair-breaking excitations. The gapless collective phonon excitation requires the smallest excitation energy in both BCS and topological superfluids. In the critical point of phase transition, the phonon excitation is overlapped with a gapless DD-type pair-breaking excitation and a finite expansion width is imparted to the phonon peak, which is a delta-like peak when far from the critical point of phase transition. For a larger transferred momentum q, the strength of the phonon excitation gradually decreases and merges into the pair-breaking excitation regime, and the excitation signals in both density and spin dynamic structure factors are dominated by single-particle excitation, including three kinds of
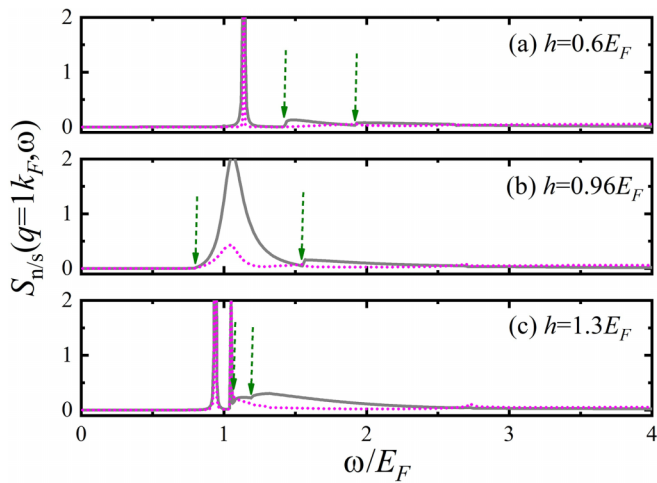

FIG. 7. The density (gray line) and spin (magenta line) dynamical structure factors at the transferred momentum $q = 1k_F$. The parameters in these three panels are the same as those in Fig. 5.
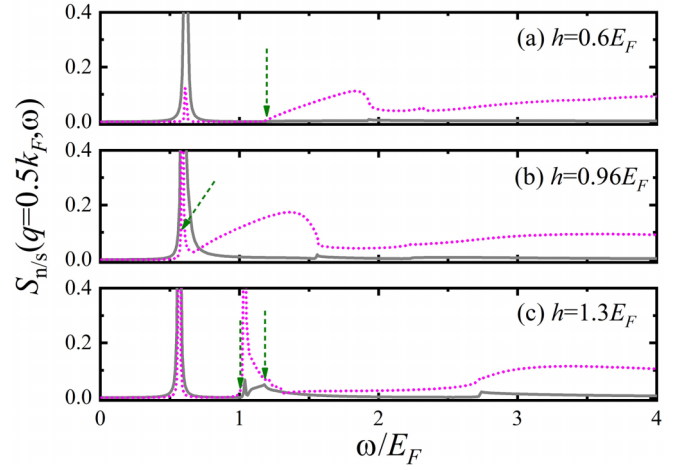
pair-breaking excitation, and two-atom molecular and single atomic excitations. The two-atom molecular (single atomic) excitations can be well explained by an ideal single molecule (atom) dispersion relation at a very large transferred momentum $\boldsymbol{q} \gg k_F$. Our research on the dynamic structure factor can help us to understand the dynamical excitation information in both BCS and topological matter states, distinguish different matter states during phase transition, and judge the location of phase transition.

In the near future, it will be interesting to bring some nonuniform structures, like edge, impurity, or soliton (vortex), to this system, with the expectation of investigating some excitations related to the generation of Majorana fermions [52–55], which is absent in the current work. Experimentally the edge can be brought by a hard wall or a harmonic trap, and the soliton can be generated by a phase-imprinting technique [56]. So it will be worth carrying out calculation of these nonuniform systems.

ACKNOWLEDGMENTS

APPENDIX

The exact diagonalization of the mean-field Hamiltonian H_{mf} is carried out by the motion equation of the Green's function $\omega\langle\langle c_1 | c_2 \rangle\rangle = \langle [c_1, c_2]_+ \rangle + \langle\langle [c_1, H_{\mathrm{mf}}] | c_2 \rangle\rangle$, where c_1 and c_2 are any possible fermionic operators of the system, and the double-bracket notation $\langle\langle c_1 | c_2 \rangle\rangle$ is the corresponding momentum-energy Fourier transformation of the space-time Green's function $G(r_1, \tau, r_2, 0) = -\langle T \psi_1(r_1, \tau)\psi_2(r_2, 0) \rangle$. Finally, we find that the system has six independent Green's functions. In this Appendix, we list expressions of six independent Green's functions and the mean-field response function $\chi^0 = A + B$. The six independent Green's functions are $G_1(\boldsymbol{k}, \omega) = \sum_l [G_1]_{\boldsymbol{k}}^l/(\omega - E_{\boldsymbol{k}}^l)$, with

$$[G_1]_{\boldsymbol{k}}^{(1)} = \frac{U_{\boldsymbol{k}}^2 - (h^2 + \boldsymbol{k}^2\lambda^2 + E_{\boldsymbol{k}}^2 + 2h\xi_{\boldsymbol{k}})}{2(U_{\boldsymbol{k}}^2 - D_{\boldsymbol{k}}^2)}$$
$$+ \frac{(\xi_{\boldsymbol{k}} - h)U_{\boldsymbol{k}}^2 - (\xi_{\boldsymbol{k}} + h)(E_{\boldsymbol{k}}^2 - h^2 - \boldsymbol{k}^2\lambda^2)}{2U_{\boldsymbol{k}}(U_{\boldsymbol{k}}^2 - D_{\boldsymbol{k}}^2)},$$

$$[G_1]_{\boldsymbol{k}}^{(-1)} = \frac{U_{\boldsymbol{k}}^2 - (h^2 + \boldsymbol{k}^2\lambda^2 + E_{\boldsymbol{k}}^2 + 2h\xi_{\boldsymbol{k}})}{2(U_{\boldsymbol{k}}^2 - D_{\boldsymbol{k}}^2)}$$
$$- \frac{(\xi_{\boldsymbol{k}} - h)U_{\boldsymbol{k}}^2 - (\xi_{\boldsymbol{k}} + h)(E_{\boldsymbol{k}}^2 - h^2 - \boldsymbol{k}^2\lambda^2)}{2U_{\boldsymbol{k}}(U_{\boldsymbol{k}}^2 - D_{\boldsymbol{k}}^2)},$$

$$[G_1]_{\boldsymbol{k}}^{(2)} = -\frac{D_{\boldsymbol{k}}^2 - (h^2 + \boldsymbol{k}^2\lambda^2 + E_{\boldsymbol{k}}^2 + 2h\xi_{\boldsymbol{k}})}{2(U_{\boldsymbol{k}}^2 - D_{\boldsymbol{k}}^2)}$$
$$- \frac{(\xi_{\boldsymbol{k}} - h)D_{\boldsymbol{k}}^2 - (\xi_{\boldsymbol{k}} + h)(E_{\boldsymbol{k}}^2 - h^2 - \boldsymbol{k}^2\lambda^2)}{2D_{\boldsymbol{k}}(U_{\boldsymbol{k}}^2 - D_{\boldsymbol{k}}^2)},$$

$$[G_1]_{\boldsymbol{k}}^{(-2)} = -\frac{D_{\boldsymbol{k}}^2 - (h^2 + \boldsymbol{k}^2\lambda^2 + E_{\boldsymbol{k}}^2 + 2h\xi_{\boldsymbol{k}})}{2(U_{\boldsymbol{k}}^2 - D_{\boldsymbol{k}}^2)}$$
$$+ \frac{(\xi_{\boldsymbol{k}} - h)D_{\boldsymbol{k}}^2 - (\xi_{\boldsymbol{k}} + h)(E_{\boldsymbol{k}}^2 - h^2 - \boldsymbol{k}^2\lambda^2)}{2D_{\boldsymbol{k}}(U_{\boldsymbol{k}}^2 - D_{\boldsymbol{k}}^2)};$$

$$G_2(\boldsymbol{k}, \omega) = \sum_l [G_2]_{\boldsymbol{k}}^l/(\omega - E_{\boldsymbol{k}}^l), \quad \text{with}$$

$$[G_2]_{\boldsymbol{k}}^{(1)} = \frac{U_{\boldsymbol{k}}^2 - (h^2 + \boldsymbol{k}^2\lambda^2 + E_{\boldsymbol{k}}^2 - 2h\xi_{\boldsymbol{k}})}{2(U_{\boldsymbol{k}}^2 - D_{\boldsymbol{k}}^2)}$$
$$+ \frac{(\xi_{\boldsymbol{k}} + h)U_{\boldsymbol{k}}^2 - (\xi_{\boldsymbol{k}} - h)(E_{\boldsymbol{k}}^2 - h^2 - \boldsymbol{k}^2\lambda^2)}{2U_{\boldsymbol{k}}(U_{\boldsymbol{k}}^2 - D_{\boldsymbol{k}}^2)},$$

$$[G_2]_{\boldsymbol{k}}^{(-1)} = \frac{U_{\boldsymbol{k}}^2 - (h^2 + \boldsymbol{k}^2\lambda^2 + E_{\boldsymbol{k}}^2 - 2h\xi_{\boldsymbol{k}})}{2(U_{\boldsymbol{k}}^2 - D_{\boldsymbol{k}}^2)}$$
$$- \frac{(\xi_{\boldsymbol{k}} + h)U_{\boldsymbol{k}}^2 - (\xi_{\boldsymbol{k}} - h)(E_{\boldsymbol{k}}^2 - h^2 - \boldsymbol{k}^2\lambda^2)}{2U_{\boldsymbol{k}}(U_{\boldsymbol{k}}^2 - D_{\boldsymbol{k}}^2)},$$

$$[G_2]_{\boldsymbol{k}}^{(2)} = -\frac{D_{\boldsymbol{k}}^2 - (h^2 + \boldsymbol{k}^2\lambda^2 + E_{\boldsymbol{k}}^2 - 2h\xi_{\boldsymbol{k}})}{2(U_{\boldsymbol{k}}^2 - D_{\boldsymbol{k}}^2)}$$
$$- \frac{(\xi_{\boldsymbol{k}} + h)D_{\boldsymbol{k}}^2 - (\xi_{\boldsymbol{k}} - h)(E_{\boldsymbol{k}}^2 - h^2 - \boldsymbol{k}^2\lambda^2)}{2D_{\boldsymbol{k}}(U_{\boldsymbol{k}}^2 - D_{\boldsymbol{k}}^2)},$$

$$[G_2]_{\boldsymbol{k}}^{(-2)} = -\frac{D_{\boldsymbol{k}}^2 - (h^2 + \boldsymbol{k}^2\lambda^2 + E_{\boldsymbol{k}}^2 - 2h\xi_{\boldsymbol{k}})}{2(U_{\boldsymbol{k}}^2 - D_{\boldsymbol{k}}^2)}$$
$$+ \frac{(\xi_{\boldsymbol{k}} + h)D_{\boldsymbol{k}}^2 - (\xi_{\boldsymbol{k}} - h)(E_{\boldsymbol{k}}^2 - h^2 - \boldsymbol{k}^2\lambda^2)}{2D_{\boldsymbol{k}}(U_{\boldsymbol{k}}^2 - D_{\boldsymbol{k}}^2)};$$

$$\Gamma(\boldsymbol{k}, \omega) = \sum_l [\Gamma]_{\boldsymbol{k}}^l/(\omega - E_{\boldsymbol{k}}^l), \quad \text{with}$$

$$[\Gamma]_{\boldsymbol{k}}^{(1)} = +\frac{\Delta h}{U_{\boldsymbol{k}}^2 - D_{\boldsymbol{k}}^2} - \frac{\Delta[U_{\boldsymbol{k}}^2 + (h^2 - \boldsymbol{k}^2\lambda^2 - E_{\boldsymbol{k}}^2)]}{2U_{\boldsymbol{k}}(U_{\boldsymbol{k}}^2 - D_{\boldsymbol{k}}^2)},$$

$$[\Gamma]_{\boldsymbol{k}}^{(-1)} = +\frac{\Delta h}{U_{\boldsymbol{k}}^2 - D_{\boldsymbol{k}}^2} + \frac{\Delta[U_{\boldsymbol{k}}^2 + (h^2 - \boldsymbol{k}^2\lambda^2 - E_{\boldsymbol{k}}^2)]}{2U_{\boldsymbol{k}}(U_{\boldsymbol{k}}^2 - D_{\boldsymbol{k}}^2)},$$

$$[\Gamma]_{\boldsymbol{k}}^{(2)} = -\frac{\Delta h}{U_{\boldsymbol{k}}^2 - D_{\boldsymbol{k}}^2} + \frac{\Delta[D_{\boldsymbol{k}}^2 + (h^2 - \boldsymbol{k}^2\lambda^2 - E_{\boldsymbol{k}}^2)]}{2D_{\boldsymbol{k}}(U_{\boldsymbol{k}}^2 - D_{\boldsymbol{k}}^2)},$$

$$[\Gamma]_{\boldsymbol{k}}^{(-2)} = -\frac{\Delta h}{U_{\boldsymbol{k}}^2 - D_{\boldsymbol{k}}^2} - \frac{\Delta[D_{\boldsymbol{k}}^2 + (h^2 - \boldsymbol{k}^2\lambda^2 - E_{\boldsymbol{k}}^2)]}{2D_{\boldsymbol{k}}(U_{\boldsymbol{k}}^2 - D_{\boldsymbol{k}}^2)};$$

$S(\mathbf{k}, \omega) = \sum_l [S]^l_{\mathbf{k}}/(\omega - E^l_{\mathbf{k}})$, with

$$[S]^{(1)}_{\mathbf{k}} = (k_y - ik_x)\lambda \left[+\frac{\xi_{\mathbf{k}}}{U^2_{\mathbf{k}} - D^2_{\mathbf{k}}} + \frac{U^2_{\mathbf{k}} + (\xi^2_{\mathbf{k}} - h^2 - \mathbf{k}^2\lambda^2 - \Delta^2)}{2U_{\mathbf{k}}(U^2_{\mathbf{k}} - D^2_{\mathbf{k}})} \right],$$

$$[S]^{(-1)}_{\mathbf{k}} = (k_y - ik_x)\lambda \left[+\frac{\xi_{\mathbf{k}}}{U^2_{\mathbf{k}} - D^2_{\mathbf{k}}} - \frac{U^2_{\mathbf{k}} + (\xi^2_{\mathbf{k}} - h^2 - \mathbf{k}^2\lambda^2 - \Delta^2)}{2U_{\mathbf{k}}(U^2_{\mathbf{k}} - D^2_{\mathbf{k}})} \right],$$

$$[S]^{(2)}_{\mathbf{k}} = (k_y - ik_x)\lambda \left[-\frac{\xi_{\mathbf{k}}}{U^2_{\mathbf{k}} - D^2_{\mathbf{k}}} - \frac{D^2_{\mathbf{k}} + (\xi^2_{\mathbf{k}} - h^2 - \mathbf{k}^2\lambda^2 - \Delta^2)}{2D_{\mathbf{k}}(U^2_{\mathbf{k}} - D^2_{\mathbf{k}})} \right],$$

$$[S]^{(-2)}_{\mathbf{k}} = (k_y - ik_x)\lambda \left[-\frac{\xi_{\mathbf{k}}}{U^2_{\mathbf{k}} - D^2_{\mathbf{k}}} + \frac{D^2_{\mathbf{k}} + (\xi^2_{\mathbf{k}} - h^2 - \mathbf{k}^2\lambda^2 - \Delta^2)}{2D_{\mathbf{k}}(U^2_{\mathbf{k}} - D^2_{\mathbf{k}})} \right];$$

$F_1(\mathbf{k}, \omega) = \sum_l [F_1]^l_{\mathbf{k}}/(\omega - E^l_{\mathbf{k}})$, with

$$[F_1]^{(1)}_{\mathbf{k}} = -[F_1]^{(-1)}_{\mathbf{k}} = +\frac{\Delta\lambda(k_y + ik_x)(\xi_{\mathbf{k}} + h)}{U_{\mathbf{k}}(U^2_{\mathbf{k}} - D^2_{\mathbf{k}})},$$

$$[F_1]^{(2)}_{\mathbf{k}} = -[F_1]^{(-2)}_{\mathbf{k}} = -\frac{\Delta\lambda(k_y + ik_x)(\xi_{\mathbf{k}} + h)}{D_{\mathbf{k}}(U^2_{\mathbf{k}} - D^2_{\mathbf{k}})};$$

and $F_2(\mathbf{k}, \omega) = \sum_l [F_2]^l_{\mathbf{k}}/(\omega - E^l_{\mathbf{k}})$, with

$$[F_2]^{(1)}_{\mathbf{k}} = -[F_2]^{(-1)}_{\mathbf{k}} = -\frac{\Delta\lambda(k_y - ik_x)(\xi_{\mathbf{k}} - h)}{U_{\mathbf{k}}(U^2_{\mathbf{k}} - D^2_{\mathbf{k}})},$$

$$[F_2]^{(2)}_{\mathbf{k}} = -[F_2]^{(-2)}_{\mathbf{k}} = +\frac{\Delta\lambda(k_y - ik_x)(\xi_{\mathbf{k}} - h)}{D_{\mathbf{k}}(U^2_{\mathbf{k}} - D^2_{\mathbf{k}})}.$$

The expressions of all 9 independent matrix elements in the mean-field response function A are

$$A_{11} = +\sum_{pll'} [G_1]^l_{\mathbf{p}}[G_1]^{l'}_{\mathbf{p+q}} \frac{f(E^l_{\mathbf{p}}) - f(E^{l'}_{\mathbf{p+q}})}{i\omega_n + E^l_{\mathbf{p}} - E^{l'}_{\mathbf{p+q}}},$$

$$A_{12} = -\sum_{pll'} [\Gamma]^l_{\mathbf{p}}[\Gamma]^{l'}_{\mathbf{p+q}} \frac{f(E^l_{\mathbf{p}}) - f(E^{l'}_{\mathbf{p+q}})}{i\omega_n + E^l_{\mathbf{p}} - E^{l'}_{\mathbf{p+q}}},$$

$$A_{13} = +\sum_{pll'} [G_1]^l_{\mathbf{p}}[\Gamma]^{l'}_{\mathbf{p+q}} \frac{f(E^l_{\mathbf{p}}) - f(E^{l'}_{\mathbf{p+q}})}{i\omega_n + E^l_{\mathbf{p}} - E^{l'}_{\mathbf{p+q}}},$$

$$A_{14} = +\sum_{pll'} [\Gamma]^l_{\mathbf{p}}[G_1]^{l'}_{\mathbf{p+q}} \frac{f(E^l_{\mathbf{p}}) - f(E^{l'}_{\mathbf{p+q}})}{i\omega_n + E^l_{\mathbf{p}} - E^{l'}_{\mathbf{p+q}}},$$

$$A_{22} = +\sum_{pll'} [G_2]^l_{\mathbf{p}}[G_2]^{l'}_{\mathbf{p+q}} \frac{f(E^l_{\mathbf{p}}) - f(E^{l'}_{\mathbf{p+q}})}{i\omega_n + E^l_{\mathbf{p}} - E^{l'}_{\mathbf{p+q}}},$$

$$A_{23} = -\sum_{pll'} [G_2]^l_{\mathbf{p}}[\Gamma]^{-l'}_{\mathbf{p+q}} \frac{f(E^l_{\mathbf{p}}) - f(E^{l'}_{\mathbf{p+q}})}{i\omega_n + E^l_{\mathbf{p}} - E^{l'}_{\mathbf{p+q}}},$$

$$A_{24} = -\sum_{pll'} [\Gamma]^{-l}_{\mathbf{p}}[G_2]^{l'}_{\mathbf{p+q}} \frac{f(E^l_{\mathbf{p}}) - f(E^{l'}_{\mathbf{p+q}})}{i\omega_n + E^l_{\mathbf{p}} - E^{l'}_{\mathbf{p+q}}},$$

$$A_{34} = +\sum_{pll'} [G_2]^{-l}_{\mathbf{p}}[G_1]^{l'}_{\mathbf{p+q}} \frac{f(E^l_{\mathbf{p}}) - f(E^{l'}_{\mathbf{p+q}})}{i\omega_n + E^l_{\mathbf{p}} - E^{l'}_{\mathbf{p+q}}},$$

$$A_{43} = +\sum_{pll'} [G_1]^l_{\mathbf{p}}[G_2]^{-l'}_{\mathbf{p+q}} \frac{f(E^l_{\mathbf{p}}) - f(E^{l'}_{\mathbf{p+q}})}{i\omega_n + E^l_{\mathbf{p}} - E^{l'}_{\mathbf{p+q}}},$$

where $f(x) = 1/(e^{x/T} + 1)$ is the Fermi-Dirac distribution function. The expressions of the 16 independent matrix elements in the mean-field response function B are

$$B_{11} = -\sum_{pll'} [F^*_1]^l_{\mathbf{p}}[F_1]^{l'}_{\mathbf{p+q}} \frac{f(E^l_{\mathbf{p}}) - f(E^{l'}_{\mathbf{p+q}})}{i\omega_n + E^l_{\mathbf{p}} - E^{l'}_{\mathbf{p+q}}},$$

$$B_{12} = +\sum_{pll'} [S]^l_{\mathbf{p}}[S^*]^{l'}_{\mathbf{p+q}} \frac{f(E^l_{\mathbf{p}}) - f(E^{l'}_{\mathbf{p+q}})}{i\omega_n + E^l_{\mathbf{p}} - E^{l'}_{\mathbf{p+q}}},$$

$$B_{13} = -\sum_{pll'} [S]^l_{\mathbf{p}}[F_1]^{l'}_{\mathbf{p+q}} \frac{f(E^l_{\mathbf{p}}) - f(E^{l'}_{\mathbf{p+q}})}{i\omega_n + E^l_{\mathbf{p}} - E^{l'}_{\mathbf{p+q}}},$$

$$B_{14} = -\sum_{pll'} [F^*_1]^l_{\mathbf{p}}[S^*]^{l'}_{\mathbf{p+q}} \frac{f(E^l_{\mathbf{p}}) - f(E^{l'}_{\mathbf{p+q}})}{i\omega_n + E^l_{\mathbf{p}} - E^{l'}_{\mathbf{p+q}}},$$

$$B_{21} = +\sum_{pll'} [S^*]^l_{\mathbf{p}}[S]^{l'}_{\mathbf{p+q}} \frac{f(E^l_{\mathbf{p}}) - f(E^{l'}_{\mathbf{p+q}})}{i\omega_n + E^l_{\mathbf{p}} - E^{l'}_{\mathbf{p+q}}},$$

$$B_{22} = -\sum_{pll'} [F_2]^l_{\mathbf{p}}[F^*_2]^{l'}_{\mathbf{p+q}} \frac{f(E^l_{\mathbf{p}}) - f(E^{l'}_{\mathbf{p+q}})}{i\omega_n + E^l_{\mathbf{p}} - E^{l'}_{\mathbf{p+q}}},$$

$$B_{23} = +\sum_{pll'} [S^*]^l_{\mathbf{p}}[F_2]^{l'}_{\mathbf{p+q}} \frac{f(E^l_{\mathbf{p}}) - f(E^{l'}_{\mathbf{p+q}})}{i\omega_n + E^l_{\mathbf{p}} - E^{l'}_{\mathbf{p+q}}},$$

$$B_{24} = +\sum_{pll'} [F^*_2]^l_{\mathbf{p}}[S]^{l'}_{\mathbf{p+q}} \frac{f(E^l_{\mathbf{p}}) - f(E^{l'}_{\mathbf{p+q}})}{i\omega_n + E^l_{\mathbf{p}} - E^{l'}_{\mathbf{p+q}}},$$

$$B_{31} = -\sum_{pll'} [F_1]^l_{\mathbf{p}}[S]^{l'}_{\mathbf{p+q}} \frac{f(E^l_{\mathbf{p}}) - f(E^{l'}_{\mathbf{p+q}})}{i\omega_n + E^l_{\mathbf{p}} - E^{l'}_{\mathbf{p+q}}},$$

$$B_{32} = +\sum_{pll'} [F_2]^l_{\mathbf{p}}[S^*]^{l'}_{\mathbf{p+q}} \frac{f(E^l_{\mathbf{p}}) - f(E^{l'}_{\mathbf{p+q}})}{i\omega_n + E^l_{\mathbf{p}} - E^{l'}_{\mathbf{p+q}}},$$

$$B_{33} = -\sum_{\boldsymbol{p}ll'}[F_2]^l_{\boldsymbol{p}}[F_1]^{l'}_{\boldsymbol{p}+\boldsymbol{q}}\frac{f(E^l_{\boldsymbol{p}}) - f(E^{l'}_{\boldsymbol{p}+\boldsymbol{q}})}{i\omega_n + E^l_{\boldsymbol{p}} - E^{l'}_{\boldsymbol{p}+\boldsymbol{q}}},$$

$$B_{42} = +\sum_{\boldsymbol{p}ll'}[S]^l_{\boldsymbol{p}}[F_2^*]^{l'}_{\boldsymbol{p}+\boldsymbol{q}}\frac{f(E^l_{\boldsymbol{p}}) - f(E^{l'}_{\boldsymbol{p}+\boldsymbol{q}})}{i\omega_n + E^l_{\boldsymbol{p}} - E^{l'}_{\boldsymbol{p}+\boldsymbol{q}}},$$

$$B_{34} = +\sum_{\boldsymbol{p}ll'}[S]^{-l}_{\boldsymbol{p}}[S^*]^{l'}_{\boldsymbol{p}+\boldsymbol{q}}\frac{f(E^l_{\boldsymbol{p}}) - f(E^{l'}_{\boldsymbol{p}+\boldsymbol{q}})}{i\omega_n + E^l_{\boldsymbol{p}} - E^{l'}_{\boldsymbol{p}+\boldsymbol{q}}},$$

$$B_{43} = +\sum_{\boldsymbol{p}ll'}[S]^l_{\boldsymbol{p}}[S^*]^{-l'}_{\boldsymbol{p}+\boldsymbol{q}}\frac{f(E^l_{\boldsymbol{p}}) - f(E^{l'}_{\boldsymbol{p}+\boldsymbol{q}})}{i\omega_n + E^l_{\boldsymbol{p}} - E^{l'}_{\boldsymbol{p}+\boldsymbol{q}}},$$

$$B_{41} = -\sum_{\boldsymbol{p}ll'}[S^*]^l_{\boldsymbol{p}}[F_1^*]^{l'}_{\boldsymbol{p}+\boldsymbol{q}}\frac{f(E^l_{\boldsymbol{p}}) - f(E^{l'}_{\boldsymbol{p}+\boldsymbol{q}})}{i\omega_n + E^l_{\boldsymbol{p}} - E^{l'}_{\boldsymbol{p}+\boldsymbol{q}}},$$

$$B_{44} = -\sum_{\boldsymbol{p}ll'}[F_1^*]^l_{\boldsymbol{p}}[F_2^*]^{l'}_{\boldsymbol{p}+\boldsymbol{q}}\frac{f(E^l_{\boldsymbol{p}}) - f(E^{l'}_{\boldsymbol{p}+\boldsymbol{q}})}{i\omega_n + E^l_{\boldsymbol{p}} - E^{l'}_{\boldsymbol{p}+\boldsymbol{q}}}.$$

[1] I. Bloch, J. Dalibard, and W. Zwerger, Many-body physics with ultracold gases, Rev. Mod. Phys. **80**, 885 (2008).

[2] S. Giorgini, L. P. Pitaevskii, and S. Stringari, Theory of ultracold atomic Fermi gases, Rev. Mod. Phys. **80**, 1215 (2008).

[3] Y.-J. Lin, K. Jiménez-García, and I. B. Spielman, Spin–orbit-coupled Bose–Einstein condensates, Nature (London) **471**, 83 (2011).

[4] P. Wang, Z.-Q. Yu, Z. Fu, J. Miao, L. Huang, S. Chai, H. Zhai, and J. Zhang, Spin-Orbit Coupled Degenerate Fermi Gases, Phys. Rev. Lett. **109**, 095301 (2012).

[5] P.-K. Chen, L.-R. Liu, M.-J. Tsai, N.-C. Chiu, Y. Kawaguchi, S.-K. Yip, M.-S. Chang, and Y.-J. Lin, Rotating Atomic Quantum Gases with Light-Induced Azimuthal Gauge Potentials and the Observation of the Hess-Fairbank Effect, Phys. Rev. Lett. **121**, 250401 (2018).

[6] D. Zhang, T. Gao, P. Zou, L. Kong, R. Li, X. Shen, X.-L. Chen, S.-G. Peng, M. Zhan, H. Pu, and K. Jiang, Ground-State Phase Diagram of a Spin-Orbital-Angular-Momentum Coupled Bose-Einstein Condensate, Phys. Rev. Lett. **122**, 110402 (2019).

[7] L. W. Cheuk, A. T. Sommer, Z. Hadzibabic, T. Yefsah, W. S. Bakr, and M. W. Zwierlein, Spin-Injection Spectroscopy of a Spin-Orbit Coupled Fermi Gas, Phys. Rev. Lett. **109**, 095302 (2012).

[8] R. A. Williams, M. C. Beeler, L. J. LeBlanc, K. Jiménez-García, and I. B. Spielman, Raman-Induced Interactions in a Single-Component Fermi Gas near an *s*-Wave Feshbach Resonance, Phys. Rev. Lett. **111**, 095301 (2013).

[9] Z. Meng, L. Huang, P. Peng, D. Li, L. Chen, Y. Xu, C. Zhang, P. Wang, and J. Zhang, Experimental Observation of a Topological Band Gap Opening in Ultracold Fermi Gases with Two-Dimensional Spin-Orbit Coupling, Phys. Rev. Lett. **117**, 235304 (2016).

[10] N. Q. Burdick, Y. Tang, and B. L. Lev, Long-Lived Spin-Orbit-Coupled Degenerate Dipolar Fermi Gas, Phys. Rev. X **6**, 031022 (2016).

[11] L. Huang, Z. Meng, P. Wang, P. Peng, S.-L. Zhang, L. Chen, D. Li, Q. Zhou, and J. Zhang, Experimental realization of two-dimensional synthetic spin-orbit coupling in ultracold Fermi gases, Nat. Phys. **12**, 540 (2016).

[12] Z. Wu, L. Zhang, W. Sun, X.-T. Xu, B.-Z. Wang, S.-C. Ji, Y. Deng, S. Chen, X.-J. Liu, and J.-W. Pan, Realization of two-dimensional spin-orbit coupling for Bose-Einstein condensates, Science **354**, 83 (2016).

[13] Z.-Y. Wang, X.-C. Cheng, B.-Z. Wang, J.-Y. Zhang, Y.-H. Lu, C.-R. Yi, S. Niu, Y. Deng, X.-J. Liu, S. Chen, and J.-W. Pan, Realization of an ideal Weyl semimetal band in a quantum gas with 3D spin-orbit coupling, Science **372**, 271 (2021).

[14] T.-L. Ho and S. Zhang, Bose-Einstein Condensates with Spin-Orbit Interaction, Phys. Rev. Lett. **107**, 150403 (2011).

[15] M. DeMarco and H. Pu, Angular spin-orbit coupling in cold atoms, Phys. Rev. A **91**, 033630 (2015).

[16] C. Qu, K. Sun, and C. Zhang, Quantum phases of Bose-Einstein condensates with synthetic spin–orbital-angular-momentum coupling, Phys. Rev. A **91**, 053630 (2015).

[17] L. Jiang, T. Kitagawa, J. Alicea, A. R. Akhmerov, D. Pekker, G. Refael, J. Ignacio Cirac, E. Demler, M. D. Lukin, and P. Zoller, Majorana Fermions in Equilibrium and in Driven Cold-Atom Quantum Wires, Phys. Rev. Lett. **106**, 220402 (2011).

[18] K.-J. Chen, F. Wu, L. He, and W. Yi, Angular topological superfluid and topological vortex in an ultracold Fermi gas, Phys. Rev. Res. **4**, 033023 (2022).

[19] R. Han, F. Yuan, and H. Zhao, Phase diagram, band structure and density of states in two-dimensional attractive Fermi-Hubbard model with Rashba spin-orbit coupling, New J. Phys. **25**, 023011 (2023).

[20] L. Pitaevskii and S. Stringari, *Bose-Einstein Condensation* (Oxford University Press, Oxford, 2003).

[21] G. Veeravalli, E. Kuhnle, P. Dyke, and C. J. Vale, Bragg Spectroscopy of a Strongly Interacting Fermi Gas, Phys. Rev. Lett. **101**, 250403 (2008).

[22] S. Hoinka, P. Dyke, M. G. Lingham, J. J. Kinnunen, G. M. Bruun, and C. J. Vale, Goldstone mode and pair-breaking excitations in atomic Fermi superfluid, Nat. Phys. **13**, 943 (2017).

[23] H. Biss, L. Sobirey, N. Luick, M. Bohlen, J. J. Kinnunen, G. M. Bruun, T. Lompe, and H. Moritz, Excitation Spectrum and Superfluid Gap of an Ultracold Fermi Gas, Phys. Rev. Lett. **128**, 100401 (2022).

[24] R. Senaratne, D. Cavazos-Cavazos, S. Wang, F. He, Y.-T. Chang, A. Kafle, H. Pu, X.-W. Guan, and R. G. Hulet, Spin-charge separation in a 1D Fermi gas with tunable interactions, Science **376**, 1305 (2022).

[25] G. Pagano, M. Mancini, G. Cappellini, P. Lombardi, F. Schäfer, H. Hu, X.-J. Liu, J. Catani, C. Sias, M. Inguscio, and L. Fallani, A one-dimensional liquid of fermions with tunable spin, Nat. Phys. **10**, 198 (2014).

[26] A. Brunello, F. Dalfovo, L. Pitaevskii, S. Stringari, and F. Zambelli, Momentum transferred to a trapped Bose-Einstein condensate by stimulated light scattering, Phys. Rev. A **64**, 063614 (2001).

[27] R. Combescot, M. Yu. Kagan, and S. Stringari, Collective mode of homogeneous superfluid Fermi gases in the BEC-BCS crossover, Phys. Rev. A **74**, 042717 (2006).

[28] P. Kettmann, S. Hannibal, M. D. Croitoru, V. M. Axt, and T. Kuhn, Pure Goldstone mode in the quench dynamics of a confined ultracold Fermi gas in the BCS-BEC crossover regime, Phys. Rev. A **96**, 033618 (2017).

[29] H. Hu, X.-C. Yao, and X.-J. Liu, Second sound with ultracold atoms: A brief historical account, AAPPS Bull. **32**, 26 (2022).

[30] X. Li, X. Luo, S. Wang, K. Xie, X. P. Liu, H. Hu, Y.-A. Chen, X.-C. Yao, and J. W. Pan, Second sound attenuation near quantum criticality, Science **375**, 528 (2022).

[31] D. Pekker and C. Varma, Amplitude/Higgs modes in condensed matter physics, Annu. Rev. Condens. Matter Phys. **6**, 269 (2015).

[32] A. Behrle, T. Harrison, J. Kombe, K. Gao, M. Link, J.-S. Bernier, C. Kollath, and M. Köhl, Higgs mode in a strongly interacting fermionic superfluid, Nat. Phys. **14**, 781 (2018).

[33] J. Bjerlin, S. M. Reimann, and G. M. Bruun, Few-Body Precursor of the Higgs Mode in a Fermi Gas, Phys. Rev. Lett. **116**, 155302 (2016).

[34] G. M. Bruun, Long-lived Higgs mode in a two-dimensional confined Fermi system, Phys. Rev. A **90**, 023621 (2014).

[35] H. Zhao, X. Gao, W. Liang, P. Zou, and F. Yuan, Dynamical structure factors of a two-dimensional Fermi superfluid within random phase approximation, New J. Phys. **22**, 093012 (2020).

[36] G. Fan, X.-L. Chen, and P. Zou, Probing two Higgs oscillations in a one-dimensional Fermi superfluid with Raman-type spin–orbit coupling, Front. Phys. **17**, 52502 (2022).

[37] D. Phan and A. V. Chubukov, Following the Higgs mode across the BCS-BEC crossover in two dimensions, Phys. Rev. B **107**, 134519 (2023).

[38] A. J. Leggett, Number-phase fluctuations in two-band superconductors, Prog. Theor. Phys. **36**, 901 (1966).

[39] Y.-C. Zhang, S. Ding, and S. Zhang, Collective modes in a twoband superfluid of ultracold alkaline-earth-metal atoms close to an orbital Feshbach resonance, Phys. Rev. A **95**, 041603(R) (2017).

[40] R. Combescot, S. Giorgini, and S. Stringari, Molecular signatures in the structure factor of an interacting Fermi gas, Europhys. Lett. **75**, 695 (2006).

[41] P. Zou, H. Zhao, L. He, X.-J. Liu, and H. Hu, Dynamic structure factors of a strongly interacting Fermi superfluid near an orbital Feshbach resonance across the phase transition from BCS to Sarma superfluid, Phys. Rev. A **103**, 053310 (2021).

[42] Z. Gao, L. He, H. Zhao, S.-G. Peng, and P. Zou, Dynamic structure factor of one-dimensional Fermi superfluid with spin-orbit coupling, Phys. Rev. A **107**, 013304 (2023).

[43] R. Han, F. Yuan, and H. Zhao, Single-particle excitations and metal-insulator transition of ultracold Fermi atoms in one-dimensional optical lattice with spin-orbit coupling, Europhys. Lett. **139**, 25001 (2022).

[44] X.-J. Liu, L. Jiang, H. Pu, and H. Hu, Probing Majorana fermions in spin-orbit-coupled atomic Fermi gases, Phys. Rev. A **85**, 021603(R) (2012).

[45] P. W. Anderson, Random-phase approximation in the superconductivity, Phys. Rev. **112**, 1900 (1958).

[46] X.-J. Liu, H. Hu, A. Minguzzi, and M. P. Tosi, Collective oscillations of a confined Bose gas at finite temperature in the random-phase approximation, Phys. Rev. A **69**, 043605 (2004).

[47] G. Bertaina and S. Giorgini, BCS-BEC Crossover in a Two-Dimensional Fermi Gas, Phys. Rev. Lett. **106**, 110403 (2011).

[48] P. Zou, E. D. Kuhnle, C. J. Vale, and H. Hu, Quantitative comparison between theoretical predictions and experimental results for Bragg spectroscopy of a strongly interacting Fermi superfluid, Phys. Rev. A **82**, 061605(R) (2010).

[49] P. Zou, H. Hu, and X.-J. Liu, Low-momentum dynamic structure factor of a strongly interacting Fermi gas at finite temperature: The Goldstone phonon and its Landau damping, Phys. Rev. A **98**, 011602(R) (2018).

[50] E. Vitali, H. Shi, M. Qin, and S. Zhang, Visualizing the BEC-BCS crossover in a two-dimensional Fermi gas: Pairing gaps and dynamical response functions from *ab initio* computations, Phys. Rev. A **96**, 061601(R) (2017).

[51] L. He and X.-G. Huang, Superfluidity and collective modes in Rashba spin-orbit coupled Fermi gases, Ann. Phys. **337**, 163 (2013).

[52] E. Majorana, Teoria simmetrica dell' elettrone e del positrone, Nuovo Cimento **14**, 171 (1937).

[53] X. J. Liu, Impurity probe of topological superfluids in one-dimensional spin-orbit-coupled atomic Fermi gases, Phys. Rev. A **87**, 013622 (2013).

[54] Y. Xu, L. Mao, B. Wu, and C. Zhang, Dark Solitons with Majorana Fermions in Spin-Orbit-Coupled Fermi Gases, Phys. Rev. Lett. **113**, 130404 (2014).

[55] X.-J. Liu, Soliton-induced Majorana fermions in a one-dimensional atomic topological superfluid, Phys. Rev. A **91**, 023610 (2015).

[56] L. Kong, G. Fan, S.-G. Peng, X.-L. Chen, H. Zhao, and P. Zou, Dynamical generation of solitons in one-dimensional Fermi superfluids with and without spin-orbit coupling, Phys. Rev. A **103**, 063318 (2021).